JOURNAL OF MATERIALS SCIENCE 29 (1994) 2893–2902

The role of interfaces and matrix void nucleation mechanism on the ductile fracture process of discontinuous fibre-reinforced composites

S. B. BINER
Ames Laboratory, Iowa State University, Ames, IA 50011, USA

The role of fibre morphology, interface failure and void nucleation mechanisms within the matrix on the deformation and fracture behaviour of discontinuous fibre-reinforced composites was numerically investigated. The matrix was modelled using a constitutive relationship that accounts for strength degradation resulting from the nucleation and growth of voids. For the matrix, two materials exhibiting identical strength and ductility but having different void-nucleation mechanisms (stress-controlled and strain-controlled) were considered and fibres were assumed to be elastic. The debonding behaviour at the fibre interfaces was simulated in terms of a cohesive zone model which describes the decohesion by both normal and tangential separation. The results indicate that in the absence of interface failure, for a given fibre morphology the void nucleation in the matrix is the key controlling parameter of the composite strength and ductility, hence, of the fracture toughness. The weak interfacial behaviour between the fibres and the matrix can significantly increase the ductility without sacrificing strength for certain fibre morphology and for certain matrix void-nucleation mechanisms.

1. Introduction

The ductile failure of the matrix by nucleation, growth and coalescence of voids is reported to be the dominant failure mode in many metal matrix composite systems which are reinforced with particulate and whisker or discontinuous fibres [1–5]. Several studies on the mechanism of ductile fracture indicate that void nucleation can occur in two different modes (stress-controlled nucleation and strain-controlled nucleation) that depend on the local stress–strain state, the most important being the size, shape and distribution of void-nucleating intermetallic inclusions and/or dispersoids [6–9]. The nucleated voids grow in size as a function of applied strain. On the other hand, the rate of void growth is considerably influenced by the hydrostatic stress state [9–11].

Recent numerical analyses of discontinuous fibre-reinforced composites have shown that significant levels of hydrostatic stresses develop in the matrix as a consequence of constrained deformation [12–15]. Of course, the magnitude of this hydrostatic stress state depends upon the geometrical parameters of the reinforcement (e.g. diameter, length and shape) and the distribution of reinforcement within the matrix. The hydrostatic stress level within the matrix increases monotonically during the far-field loading, thereby causing the apparent flow strength and strain-hardening exponents to rise with increasing deformation. However, this build-up can be relieved by one or a combination of micromechanical mechanisms, such as (a) interface separation between the reinforcement and the matrix, (b) void nucleation and growth within the matrix, and (c) formation of intense shear bands. Therefore, apart from the geometrical parameters of the reinforcement and distribution parameters within the matrix, the interface behaviour and ductile fracture characteristics of the matrix can be controlling parameters of the strength and ductility of the composite system. A good understanding of the micromechanism of damage formation and failure could be most valuable in the design of this type of composite system through intelligent manipulation of microstructure.

In this study, in order to elucidate the role of fibre morphology, interface failure and void nucleation mechanisms within the matrix, the deformation and fracture behaviour of discontinuous fibre-reinforced composites was numerically investigated. The matrix was modelled using a constitutive relationship that accounts for strength degradation resulting from the nucleation and growth of voids, and fibres are assumed to be elastic. The debonding behaviour at the fibre interfaces was simulated in terms of a cohesive zone model which describes the decohesion by both normal and tangential separation.

2. Numerical analysis

2.1. Material model

2.1.1. Matrix material

The matrix was modelled using a constitutive relationship that accounts for strength degradation resulting from the nucleation and growth of micro-voids. The basis for the constitutive model is a flow potential

introduced by Gurson [16, 17], in which voids are represented in terms of a single internal variable, f, the void volume fraction

$$\phi = \frac{\sigma_e^2}{\sigma_m^2} + 2f^* q_1 \cosh\left(\frac{q_2\sigma_h}{2\sigma_m}\right) - 1 - q_1^2 f^{*2} = 0 \quad (1)$$

where

$$\sigma_e = \tfrac{3}{2}\sigma' : \sigma', \quad \sigma_h = I:\sigma, \quad \sigma' = \sigma - \tfrac{1}{3}\sigma_h I \quad (2)$$

and σ_m is the flow strength of the matrix. The parameters q_1 and q_2 were introduced by Tvergaard [18, 19] in order to provide a better relationship between unit-cell analysis and Equation 1; the case $q_1 = q_2 = 1$ corresponds to Gurson's original formulation.

The function f^* was proposed by Tvergaard and Needleman [20] to account for the effect of rapid void coalescence at failure. Initially $f^* = f$ as originally proposed by Gurson, but at some critical void fraction, f_c, the dependence of f^* on f is changed. This function is expressed by

$$f^* = \begin{cases} f & f \le f_c \\ f_c + \dfrac{f_u^* - f_c}{f_f - f_c}(f - f_c) & f \ge f_c \end{cases} \quad (3)$$

The constant f_u^* is the value of f^* at zero stress in Equation 1 (i.e. $f_u^* = 1/q_1$) and f_f is the void fraction at fracture. As $f \to f_f$, $f^* \to f_u^*$ and the material loses all stress-carrying capacity.

The increase in void volume fraction, f, arises from the growth of existing voids and from the nucleation of new voids. Thus

$$\dot{f} = (\dot{f})_{\text{growth}} + (\dot{f})_{\text{nucleation}} \quad (4)$$

The growth rate is related to the macroscopic dilation rate by

$$(\dot{f})_{\text{growth}} = (1 - f)\delta^{ij}\dot{\eta}_{ij}^p \quad (5)$$

where $\dot{\eta}_{ij}^p$ is the plastic part of the rate of deformation.

The increase in the void volume fraction due to the nucleation process is assumed to occur in two different modes.

(i) Strain-controlled nucleation

$$(\dot{f})_{\text{nucleation}} = D\dot{\varepsilon}_m^p \quad (6)$$

Void nucleation is assumed to follow a normal distribution as suggested by Chu and Needleman [21]. Thus, plastic strain-controlled nucleation is specified by

$$D = \frac{f_N}{s_N(2\pi)^{1/2}} \exp\left[-\frac{1}{2}\left(\frac{\varepsilon_m^p - \varepsilon_N}{s_N}\right)^2 \right] \quad (7)$$

where f_N is the volume fraction of void nucleating particles, ε_N is the mean strain for nucleation, ε_m^p is the current value of effective plastic strain, and S_N is the corresponding standard deviation.

(ii) Stress-controlled nucleation

$$(\dot{f})_{\text{nucleation}} = B(\dot{\sigma}_m + \dot{\sigma}_h/3) \quad (8)$$

with

$$B = \frac{f_N}{s_N(2\pi)^{1/2}} \exp\left\{ -\frac{1}{2}\left(\frac{(\sigma_m + \sigma_h/3) - \sigma_N}{s_N}\right)^2 \right\} \quad (9)$$

where σ_N is the mean stress for nucleation and f_N and S_N have the same meaning as in Equation 7.

In the present investigation, a rate-sensitive version of Gurson's model was employed. In the matrix, the microscopic effective plastic strain rate, $\dot{\varepsilon}_m^p$, is represented by the power law relation

$$\dot{\varepsilon}_m^p = \dot{\varepsilon}_0 \left[\frac{\sigma_m}{g(\varepsilon_m^p)}\right]^{\frac{1}{m}} \quad (10)$$

where m is the strain-rate hardening exponent, $\dot{\varepsilon}_0$ is a reference strain rate, and ε_m^p is the current value of the effective plastic strain representing the actual microscopic strain state in the matrix. The function $g(\varepsilon_m^p)$ represents the effective tensile flow stress in the matrix material in a tensile test carried out at strain rate that is equal to reference strain rate, $\dot{\varepsilon}_0$. For a power-hardening matrix material the function $g(\varepsilon_m^p)$ is taken to be

$$g(\varepsilon_m^p) = \sigma_0\left(\frac{E_m\varepsilon_m^p}{\sigma_0} + 1\right)^N \quad g(0) = \sigma_0 \quad (11)$$

with strain-hardening exponent N, Young's modulus E_m and reference stress σ_0.

Using $\Phi = 0$ as the plastic potential together with the consistency condition, the values f and σ_m can be determined from the known strain rates and the macroscopic stress-rates; full formulation can be found elsewhere [13, 20, 22].

During the analyses, two composite types will be investigated: one having a matrix which fails with stress-controlled void nucleation, and the other having a matrix which fails with strain-controlled nucleation. However, the material parameters appearing in the above formulation will be adjusted such a way that both matrices will have the same strength and ductility. This condition was achieved with the following material parameters. For the matrices, the parameters appearing in Equations 10 and 11 were chosen as $E_m = 500\sigma_0$, $\nu = 0.3$, $N = 0.1$, $m = 0.01$ and the reference strain rate, $\dot{\varepsilon}_0 = 2 \times 10^{-3}$. The parameters appearing in Equations 6–9 for void nucleation were taken as $f_N = 0.04$, $s_N = 0.1$, $\sigma_N = 2.2\sigma_0$, and $\varepsilon_N = 0.3$. For accelerated void growth, the parameters appearing in Equation 3 were chosen as $f_f = 0.25$, $f_c = 0.10$ and $f_u^* = 1/1.25$. Also, $q_1 = 1.25$ and $q_2 = q_1^2$ were selected for Equation 1. The results from the separate simulations of a uniaxial tensile test sample with these parameters are shown in Figs 1 and 2. For both nucleation mechanisms the evolution of the damage at the centre of the sample with increasing deformation is given in Fig. 1. The initial discrepancy between the two nucleation mechanisms is due to the fact that for each mechanism the maximum damage occurs at different locations before the neck development. With the development of the neck, the maximum hydrostatic stress shifts to the centre of the sample and

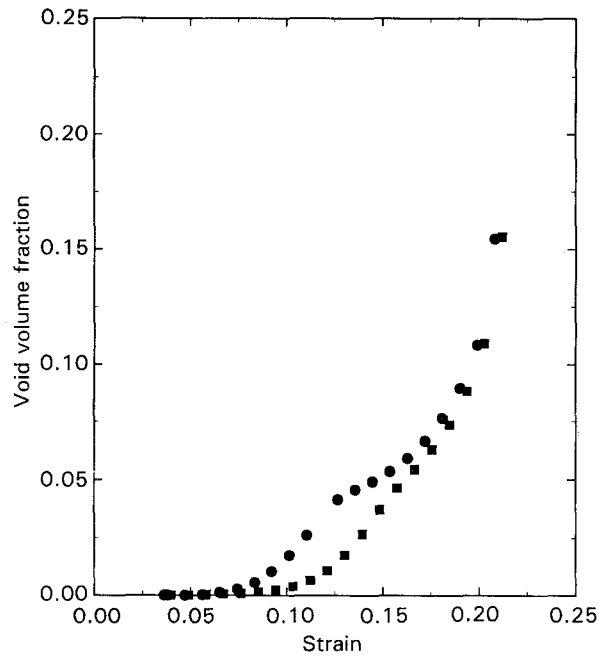

Figure 1 The damage evolution in the centre of a simulated uniaxial tensile test specimen for (●) stress-controlled and (■) strain-controlled void-nucleation models.

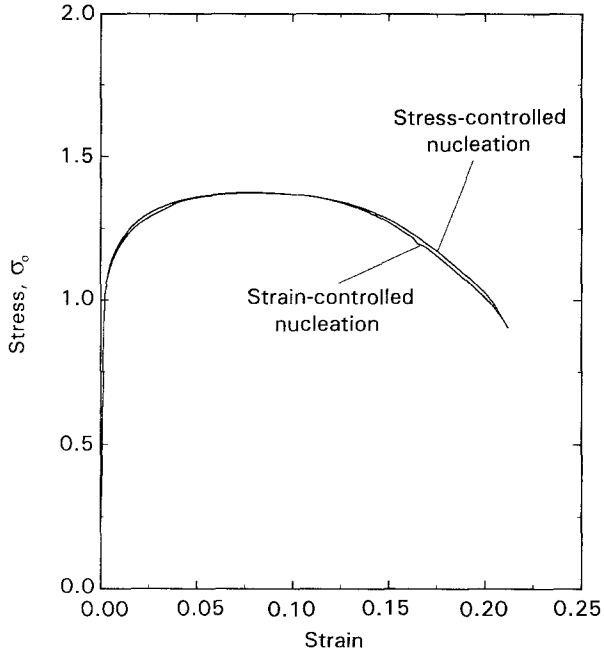

Figure 2 The resulting stress–strain curves from the simulated uniaxial tensile tests for stress-controlled and strain-controlled void-nucleation mechanisms.

subsequent increase in the damage becomes very similar. The resulting stress–strain curves from these simulations are shown in Fig. 2 and, as can be seen, they are almost identical in terms of the development of strength and ductility.

2.1.2. Fibre material

The fibre material is assumed to be linear-elastic. Young's modulus and Possion's ratio of the fibres were taken as $E_f = 10E_m$ and $\nu = 0.3$, respectively.

2.2. Interface model

To study the effects of fibre debonding and subsequent fibre pull-out during the deformation of fibre-reinforced composites, it is necessary to simulate the interface failure by normal and tangential separation. A debonding model has been developed by Needleman [23], in terms of a potential that specifies the dependence of interface traction on the displacement differences at the interface. The potential used by Needleman, which defines the non-linear variation of interface traction as a function of interface displacements, also contains three parameters σ_i, δ_i (δ_N, δ_T) and α, where σ_i is the interfacial strength; complete separation is assumed to occur at $u_N = \delta_N$; and α specifies the ratio of shear to normal stiffness of the interface. These parameters are assumed to be intrinsic material properties. However, as discussed by Tvergaard [24], the interface constitutive relationship given by Needleman [23] describes the debonding only by normal separation. Therefore, it is not suitable for tangential separation and fibre pull-out that occur under significant normal compression. An alternative model introduced by Tvergaard [24] is utilized in this study. The normal and tangential traction between the fibre and the matrix are given by

$$T_N = \frac{u_N}{\delta_N} F(\lambda) \tag{12}$$

$$T_T = \alpha \frac{u_T}{\delta_T} F(\lambda) \tag{13}$$

where $F(\lambda)$ is chosen as

$$F(\lambda) = \frac{27}{4}\sigma_i(1 - 2\lambda + \lambda^2) \quad \text{for} \quad 0 \leq \lambda \leq 1 \tag{14}$$

and

$$\lambda = \left[\left(\frac{u_N}{\delta_N}\right)^2 + \left(\frac{u_T}{\delta_T}\right)^2\right]^{1/2} \tag{15}$$

Equations 12 and 13 are valid as long as λ is monotonically increasing. In purely normal separation ($u_T \equiv 0$) the variation in the normal traction with interface separation distance is shown in Fig. 3. The maximum traction is σ_i, total separation occurs at $u_N = \delta_i$ and the work of separation per unit interface area is $9\sigma_i\delta_i/16$. In purely tangential separation ($u_N \equiv 0$), the maximum traction is $\alpha\sigma_i$, total separation occurs $u_T = \delta_i$ and the work of separation per unit area is $9\alpha\sigma_i\delta_i/16$.

For decreasing λ, a type of elastic unloading is imposed to simulate the partly damaged interface. For $\lambda \leq \lambda_{max}$ or $\lambda \leq 0$

$$T_N = \frac{u_N}{\delta_N} F(\lambda_{max}) \tag{16}$$

$$T_T = \alpha \frac{u_T}{\delta_T} F(\lambda_{max}) \tag{17}$$

If Equations 12 and 13 were used instead of Equations 16 and 17, this would mean that partly damaged material repaired itself when the loading was reversed. However, elastic springs with a large stiffness are used

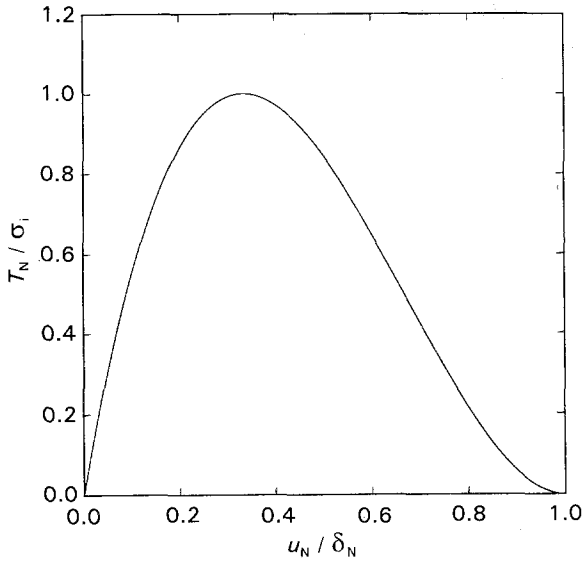

Figure 3 Schematic representation of the variation in interface strength with interface separation.

to approximately represent the contact instead of Equations 16 and 17. During the analysis, interface parameters were chosen as $\sigma_i = 2.5\sigma_0$, $\delta_N = \delta_T = 5 \times 10^{-4} r_f$ and $\alpha = 1$, and r_f is the fibre radius.

2.3. Unit-cell model

In the analysis of a deforming two-phase material, it is often necessary to make simplifying assumptions about the shape and distribution of the phases in order to make the problem tractable. A unit-cell around the periodic array of aligned discontinuous fibres as shown in Fig. 4a was approximated by an axisymmetric model as shown in Fig. 4b. Initial cell and fibre geometry were specified by cell half length, l_c, and cell radius, r_c; fibre half length, l_f, and fibre radius, r_f. The fibre volume fraction is

$$V_f = \frac{r_f^2 l_f}{r_c^2 l_c} \tag{18}$$

The initial fibre aspect ratio, a_f, and cell aspect ratio, a_c, are defined by

$$a_f = \frac{l_f}{r_f}, \quad a_c = \frac{l_c}{r_c} \tag{19}$$

The deformation of the unit-cell must be constrained to maintain the compatibility and equilibrium with the adjacent material. This constraint requires that the cell boundaries remain straight and orthogonal, and free of shear traction. Several methods for imposing these requirements on FEM models have been suggested [18, 25, 26]; the procedure outlined by Smelser and Becker [26] utilized in this study.

A typical mesh used during the analysis is shown in Fig. 4c. The elements used are quadrilaterals each built up of four triangular axisymmetric linear displacement elements. The ductile fibres constitute 20% of the total cell volume (i.e. $V_f = 0.20$) and cell aspect ratio was chosen as $a_c = 5$. Fibre aspect ratio, a_f, was varied between 2.5 and 10. The axial deformation rate of the unit cell was the same as the reference strain rate

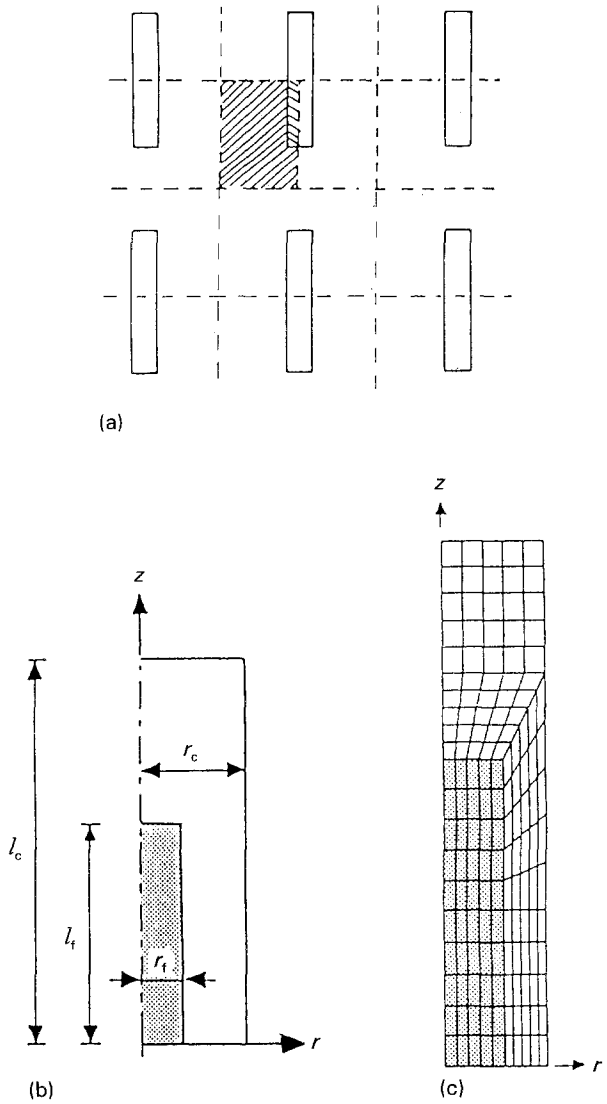

Figure 4 (a) The unit-cell. (b) The parameters of the unit-cell. (c) The typical FEM mesh used during the analysis.

in Equation 10. During the analysis, the uniform stress and strain values were computed from the resulting reaction forces and axial displacements. The integration of the stress rate requires small time steps for stable numerical integration. The tangent modulus method of Peirce *et al.* [22] is used to increase the stable time step size. The tangent modulus provides a forward gradient estimate of the deformation rate based on a Taylor series expansion about the current deformation rate.

The material failure in the matrix is implemented by element vanish technique [13]. When the failure condition is met within an element, i.e. $f \geq f_f$, that element no longer contributes to the virtual work. To avoid numerical instabilities, the nodal forces arising from the remaining stresses in failed elements are redistributed in several iterations.

3. Results

The strengthening behaviour of the composite system in the absence of any interface failure between the fibres and the matrix (i.e. rigid interface) and without any damage development in the form of nucleation and growth of voids within the matrix is considered

first. For a constant volume fraction of reinforcement $V_f = 0.20$, the effect of fibre aspect ratios of 2.5, 5 and 10 on the strengthening behaviour is given in Fig. 5 together with the strength data of unreinforced matrix material. As can be seen, the most significant increases occur in the modulus of elasticity, in the strain-hardening characteristics and in the ultimate strength of the composite with increasing aspect ratio of the discontinuous fibres. The increase in the initial yield strength (proportionality limit) occurs to a lesser extent. For these cases, the distribution of the axial stress component within the unit-cell, and the distribution of hydrostatic stress only within the matrix are shown in Figs 6 and 7, respectively. The axial stress carried by the fibres increases with increasing aspect ratio of the fibres. Near the fibre ends within the matrix, the development of large axial stress components caused by the stress concentration effect of sharp corners of the fibres can also be seen in Fig. 6. The increase in the initial yield strength of the composite to a lesser extent than the other strength parameters is associated with this early stress elevation in the matrix near the fibre ends. The magnitude of the hydrostatic stress within the matrix also increases with increasing

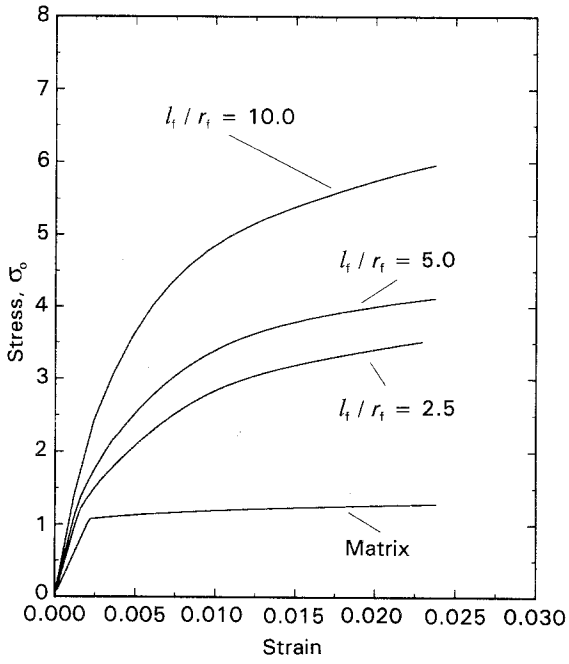

Figure 5 Variation of the stress–strain behaviour of the composite with variation in the geometrical parameters of discontinuous fibres, in the absence of any operating damage mechanism.

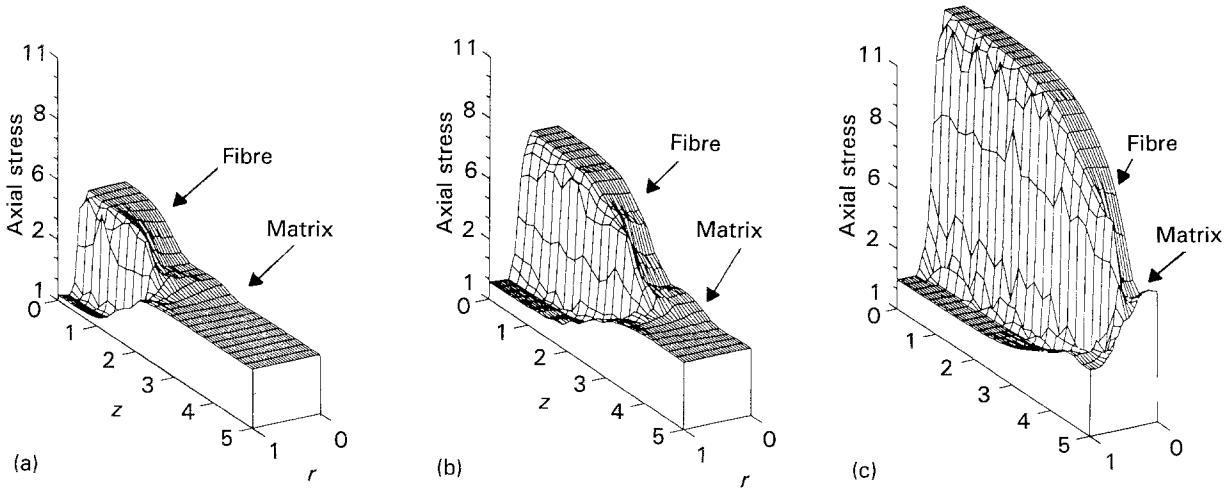

Figure 6 Variation of axial stress within the unit-cell with different fibre aspect ratios, in the absence of any damage development. $\varepsilon = 0.004$.

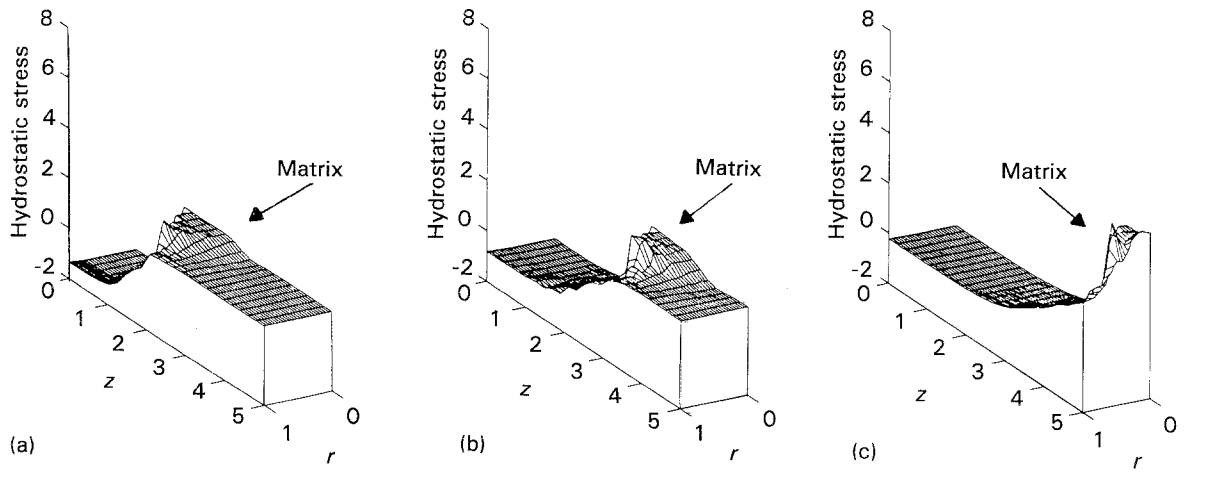

Figure 7 Variation of hydrostatic stress in the matrix with different fibre aspect ratios in the absence of any damage development. $\varepsilon = 0.004$.

fibre aspect ratio, Fig. 7. The increase in the strain hardening and flow strength seen in Fig. 5 are the result of this build-up in the hydrostatic stress which lowers the equivalent stress level, rather than the stress portioning between the fibres and the matrix. Therefore, the predictions based on only the volume fraction without taking into account the geometrical parameters of the reinforcement and their distribution, such as simple "rule of mixtures", usually fail to estimate accurately the strength characteristics of this type of composite.

In the next set of calculations, the interface between the fibres and matrix was assumed to be rigid and the nucleation and growth of the voids within the matrix was the sole damage mechanism. Two modes of void nucleation mechanisms were separately investigated and these analyses were again carried out for the three fibre aspect ratios. The resulting stress–strain curves, together with the strength data in the absence of any damage development in the composite, are given in Figs 8–10. When no damage mechanism is operative, the composite flow strength increases continuously with increasing deformation. Owing to the damage development in the matrix, in the form of nucleation and growth of voids, the strength data exhibit a maximum; and with void coalescence (i.e. by the attainment of critical void fraction $f \geq f_f$) a rapid drop occurs in the strength data. This large drop in the stress-carrying capacity is assumed to be the failure strain and is taken as a measure of the ductility of the composite during the analyses. As can be seen for both nucleation mechanism with increasing fibre aspect ratio there were slight increases in the composite strength. These slight increases in the strength were accompanied by large reductions in the ductility. At fibre aspect ratio of 2.5, the failure strains of 0.0122 and 0.0166 for stress-controlled and strain-controlled

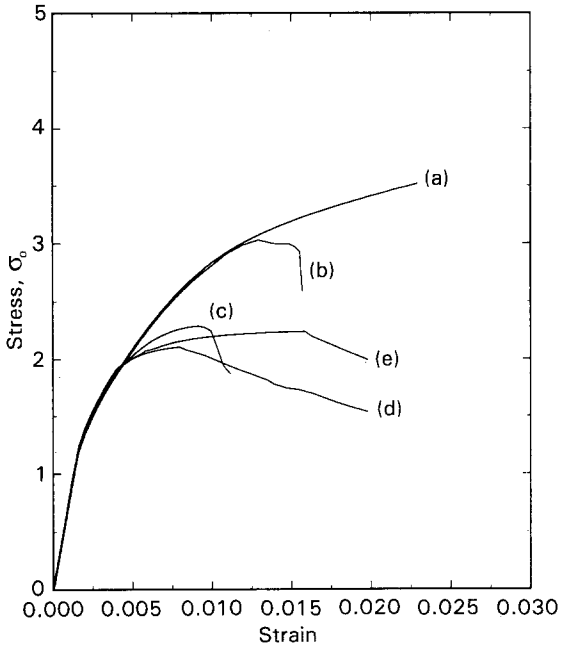

Figure 8 Stress–strain behaviour of a composite in the presence of matrix and interface failure. Data for fibre aspect ratio of 2.5. (a) No damage, (b) strain control, (c) stress control, (d) strain control and interface failure, (e) stress control and interface failure.

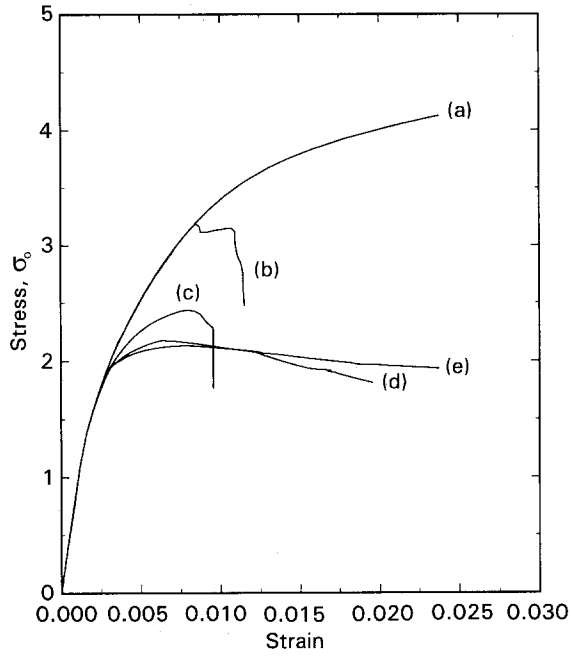

Figure 9 Stress–strain behaviour of a composite in the presence of matrix and interface failure. Data for fibre aspect ratio of 5. (a–e) See Fig. 8.

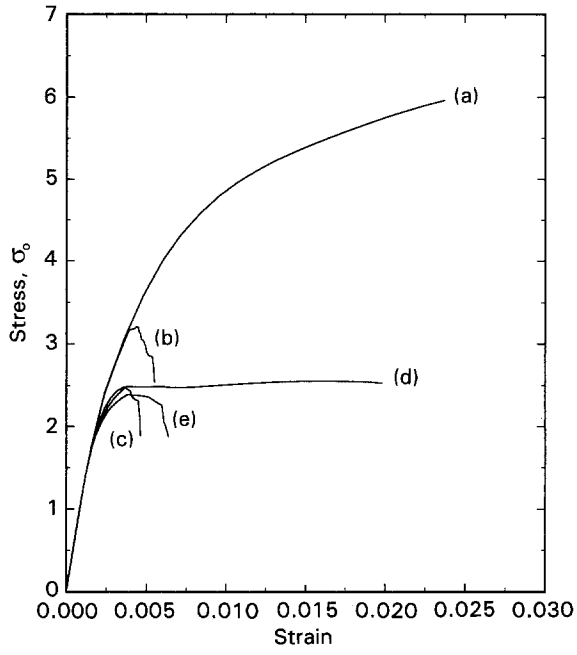

Figure 10 Stress–strain behaviour of a composite in the presence of matrix and interface failure. Data for fibre aspect ratio of 10. (a–e) See Fig. 8.

nucleation mechanisms, respectively, were dropped to 0.0044 and 0.006 at fibre aspect ratio of 10. In particular, for the largest fibre aspect ratio, very little of the matrix work-hardening capacity was utilized before the failure. For all the fibre aspect ratios investigated, the composites having the matrix with strain-controlled nucleation mechanism exhibited higher strength and ductility even though the strength and ductility behaviours of the matrices were almost indentical, Figs 1 and 2. From these results, the role of the matrix void-nucleation mechanism on the composite strength and ductility can be clearly seen.

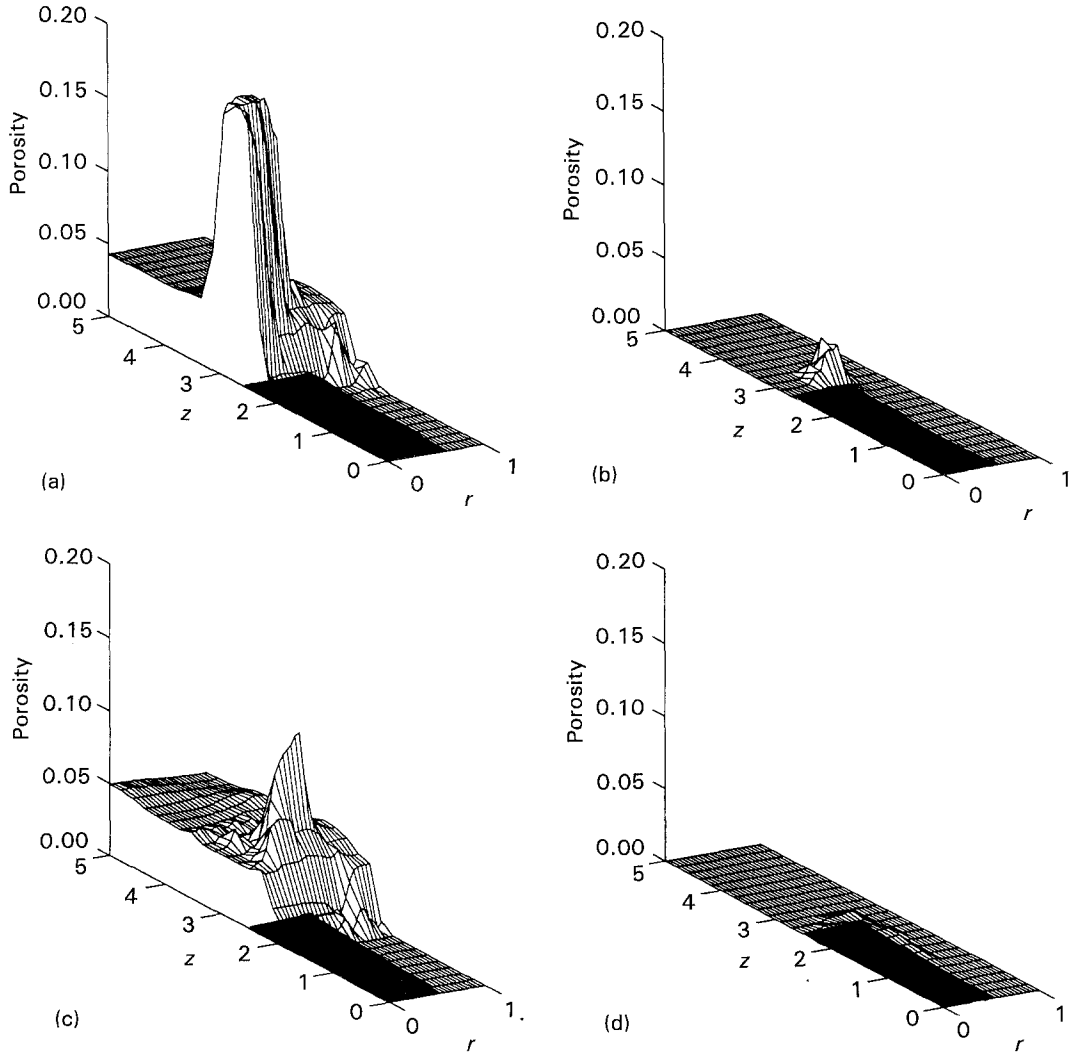

Figure 11 Damage evolution within the matrix for fibre aspect ratio of 5, for different void nucleation mechanisms and interface failure. The dark areas are the fibres. (a) Stress-controlled void nucleation, $\varepsilon = 0.010$; (b) strain-controlled void nucleation, $\varepsilon = 0.012$; (c) stress-controlled void nucleation plus interface failure, $\varepsilon = 0.024$; and (d) strain-controlled void nucleation plus interface failure, $\varepsilon = 0.020$.

In the following simulations, the role of interface separation between the fibres and the matrix is investigated. Irrespective of fibre aspect ratio and matrix failure mechanism, the interface failure started first at the top surface of the fibres. After complete separation of the top surface, the fibre pull-out progressively occurred by the debonding of side surfaces. For comparison purposes, the resulting stress–strain data from these simulations are also summarized in Figs 8–10. The interface separation had little effect on the strength behaviour of composite failing with stress-controlled nucleation mechanism. On the other hand, for this failure mechanism the ductility of the composite was significantly increased, particularly for small fibre aspect ratios. For the strain-controlled nucleation, interface failure resulted in much larger reductions in strength than its stress-controlled counterpart. Also, larger increases in the ductility of the composite were observed for increasing fibre aspect ratios.

For a fibre aspect ratio of 5 the damage evolutions within the matrix for the different nucleation mechanisms and interface failure are shown in Fig. 11. The other fibre aspect ratios investigated exhibited trends identical to those seen in Fig. 11. Either in the presence or absence of interface failure, the area fraction of matrix material undergoing damage formation was much smaller in strain-controlled than in stress-controlled nucleation due to the localization of the plastic flow. For both nucleation mechanisms, the role of interface separation can be clearly seen. In stress-controlled nucleation, the areas which exhibit a higher amount of void growth shifted away from the fibre ends. Similarly, in strain-controlled nucleation, reduction in the damage levels and the spread of the void nucleation to the regions along the fibre length due to fibre pull-out can be observed.

The overall damage, resulting from the nucleation and growth of voids in the matrix plus the void growth as a result of the interface separation is approximated as

$$\ln\left(\frac{v}{v_0}\right) = \ln\left(\frac{l}{l_c}\right) + 2\ln\left(\frac{r}{r_c}\right) - \frac{1 - 2\nu}{E_m}\sigma_h \quad (20)$$

where l and r are the current dimensions of the unit-cell and σ_h is the average hydrostatic stress. Equation 20 is approximate because of the omission of the elastic response of the fibres and of the interface displacements before the final separation. These results are summarized in Figs 12–14 for the different fibre

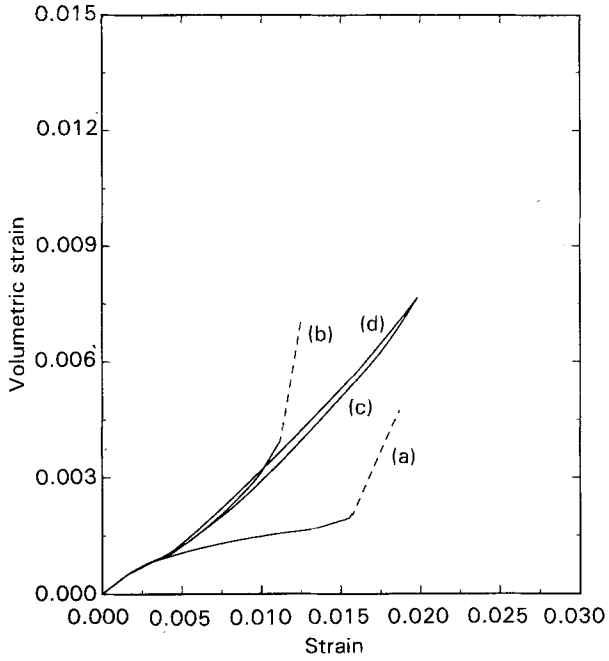

Figure 12 Variation of volumetric strain with axial strain due to the damage development in the composite. Data for fibre aspect ratio of 2.5. (a) Strain control, (b) stress control, (c) strain control and interface failure, (d) stress control and interface failure.

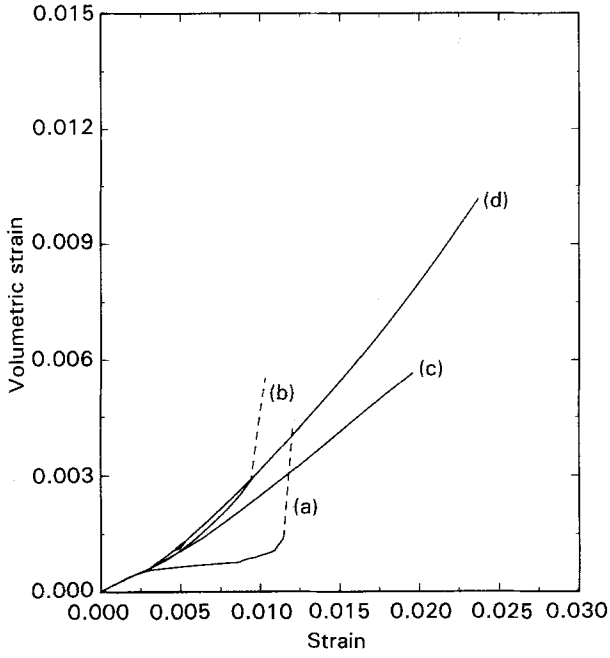

Figure 13 Variation of volumetric strain with axial strain due to the damage development in the composite. Data for fibre aspect ratio of 5. (a–d) See Fig. 12.

aspect ratios. For rigid interfaces between the fibres and the matrix, the overall total damage accumulation is faster in the case of stress-controlled void-nucleation mechanism due to large-scale void nucleation, Fig. 11. However, in this case, a limited amount of stable void growth took place due to the relaxation in the hydrostatic stress-state resulting from this large-scale void nucleation. In the case of strain-controlled nucleation, void nucleation on a much smaller scale occurred as a result of localization of the plastic flow, Fig. 11. The failure became imminent after the nucleation due to large build-up in the hydrostatic stress-state. In the case of interface failure, the initial damage accumulation in the stress-controlled void-nucleation mechanism is slightly larger than the rigid interface for fibre aspect ratios of 2.5 and 5.0, Figs 12 and 13. In these cases the interface separation took place at the same time with the damage evolution in the matrix. At this stage, matrix strain-hardening capacity was already exhausted due to the damage formation within the matrix. Therefore, for these cases there was a slight drop in the composite strength in comparison to the rigid interface, Figs 8 and 9. However, the composite ductility was significantly increased due to the larger reduction in the hydrostatic stress and also due to shift in the damage locations with the interface separation, Fig. 11. For the aspect ratio of 10 as can be seen from Fig. 14, the interface failed at a very late stage of matrix damage evolution; therefore, the improvements in the ductility were not as large as in the other two fibre aspect ratios. In the case of strain-controlled nucleation mechanism the interface failure always took place before significant damage evolution within the matrix. This can be seen as larger increases in the initial damage formation at early stages of deformation, Figs 12–14. For this case the large reductions in the composite strength (Figs 8–10) are associated with the matrix work hardening because it was not fully utilized before the interface separation. These changes in the damage morphology, with resulting variations in the strength and ductility (Figs 8–10) are the direct result of the reduction and redistribution of hydrostatic stress within the matrix due to the interface separation. However, as can be seen, the void-nucleation mechanism still plays a significant role, for the timing of the interface separation for maximum composite strength and ductility.

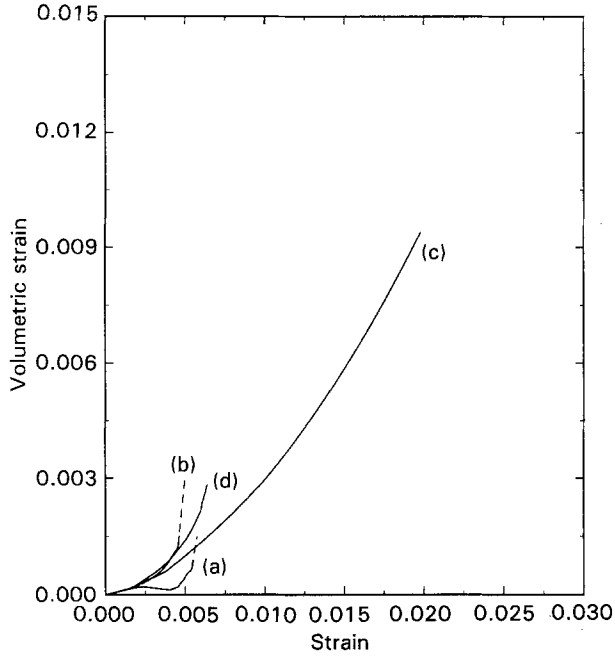

Figure 14 Variation of volumetric strain with axial strain due to the damage development in the composite. Data for fibre aspect ratio of 10. (a–d) See Fig. 12.

If the area under the stress–strain curve (work of fracture) is assumed to be the indicator of the fracture

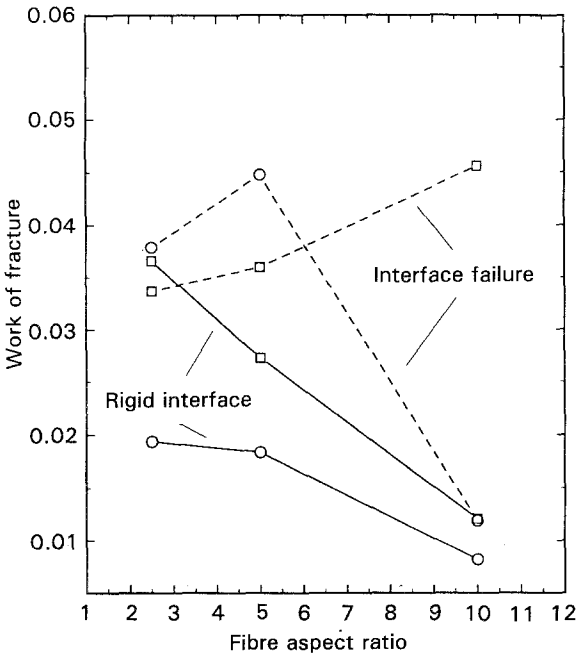

Figure 15 Variation of composite work of fracture with fibre aspect ratio, for different matrix void-nucleation mechanisms and interface failure. (○) Stress-controlled nucleation, (□) strain-controlled nucleation.

toughness, these variations for stress-controlled and strain-controlled nucleation mechanisms are given in Fig. 15. It should be mentioned that some of the simulations were terminated at about 0.02 strain level without any void coalescence (i.e. $f \leq f_f$). From the figure it can be seen that weak interface characteristics or interface failure could increase the fracture toughness significantly. However, this increase is a strong function of the matrix failure characteristics and fibre aspect ratio. For example, while significant increase occurred in the work of fracture values for small fibre aspect ratio in stress-controlled nucleation, a large increase was observed for larger fibre aspect ratios only in strain-controlled failure mechanism.

4. Discussion

The analyses presented in this study are not based on detailed quantitative data for the parameters that appear in the constitutive model of the ductile matrices and the fibres or the parameters in the cohesive zone model of a particular composite system. Rather, the results give mainly qualitative information about the influence of various parameters on the deformation and fracture behaviour of such composite system. However, in the absence of any damage mechanism, the evolution of strength due to the variation in the geometrical parameters of the fibres as seen in Fig. 5 closely follows the trends seen in experimental observations [1–5].

In the case of rigidly bonded fibres for both void-nucleation mechanisms, a slight increase in the strength and considerable reductions in the ductility were observed with increasing fibre aspect ratio, Figs 8–10. This behaviour is associated with the larger build-up in the hydrostatic stress state with increasing fibre aspect ratios as in Fig. 7. On the other hand, for a given fibre morphology, the composite behaviour was significantly different for the matrix failure mechanisms even though the matrices have the same strength and ductility characteristics, Figs 1 and 2. In case of stress-controlled nucleation mechanism, a large-scale void nucleation took place as can be seen in Fig. 11. In comparison to the strain-controlled nucleation case, the growth rate of the nucleated voids was slower (Figs 12–14), resulting from some relaxation in the hydrostatic stress state due to this extensive void nucleation. The effects of this relaxation were subsequently mitigated as the regions over which $f \geq f_f$ expanded more rapidly (i.e. fulfillment of the failure criterion) resulting again from this large-scale void nucleation. In the case of strain-controlled nucleation mechanism, the void nucleation occurred in the regions where the plastic flow was localized. Therefore, the evolution of the damage was delayed until development of this localization of plastic flow. In this case, the void nucleation was followed by very rapid growth and coalescence due to the presence of a large hydrostatic stress state. This slight delay and localization of the nucleation were the reasons for the higher strength and ductility for the composites having a matrix with the strain-controlled nucleation mechanism. From these results, it appears that for composites having rigid interfaces between the fibres and matrix, the void nucleation is the key controlling parameter of the composite strength and ductility, hence, the fracture toughness of the composite.

By fibre debonding and fibre pull-out mechanisms, the build-up in the hydrostatic stress state can be relaxed considerably. As a result of this, it can be seen that the damage tolerance of the composite increases significantly (Figs 8–10). The ductility in this case appears to be controlled by the void growth. The results clearly indicate that the toughness can be increased significantly without extensively sacrificing the strength by controlling the interface behaviour. However, it also appears that the weakening of the interface does not have the same effectiveness for all fibre geometries and matrix characteristics, Fig. 15. As can be seen this can only be effectively utilized for certain fibre morphologies and for certain void-nucleation mechanisms of the matrix. The failure of the fibres is not considered in this study; however, similar analogies to interface failure could also be made for the fibre failure cases.

Finally, in the unit-cell analysis, the assumptions of fully aligned fibres and completely periodic pattern of distribution are an idealization. Because, in general, the geometric parameters of the fibres and their distribution in the matrix are non-uniform, neither the matrix failure nor the interface failure occurs simultaneously at all locations. The residual stresses due to the large differences in the thermal expansion coefficients of the phases were also neglected during the analyses. In spite of these simplifications, it is expected that the present analyses give reasonable indications of the role of the fibre geometry, interface and matrix characteristics on the deformation and fracture behaviour of this type of composite system.

5. Conclusions

The role of fibre morphology, interface failure and void nucleation mechanisms within the matrix on the deformation and fracture behaviour of discontinuous fibre-reinforced composites was investigated. The results indicate that:

1. in the absence of interface failure, for a given matrix failure mechanism, the fibre morphology strongly affects the strength and ductility of the discontinuous fibre-reinforced composites;

2. in the absence of interface failure, for a given fibre morphology, the void nucleation in the matrix appears to be the key controlling parameter of the composite strength and ductility, and hence, of the fracture toughness. Therefore, mechanical behaviour of the composite is strongly influenced by the matrix failure mechanism;

3. the weak interfacial behaviour can significantly increase the ductility without sacrificing strength for certain fibre morphology and for certain matrix void-nucleation mechanisms.

Acknowledgements

This work was performed for the United States Department of Energy by Iowa State University under contract W-7405-Eng-82. This research was supported by the Director of Energy Research, Office of Basic Energy Sciences. The author thanks R. Winther for useful discussions during the computer implementation of the FEM model.

References

1. T. CHRISTMAN and S. SURESH, *Mater. Sci. Eng.* **102A** (1988) 221.
2. C. P. YOU, A. W. THOMPSON and I. M. BERNSTEIN, *Scripta Metall.* **21** (1987) 181.
3. S. V. NAIR, J. K. TIEN and B. C. BATES, *Int. Metall. Rev.* **30** (1985) 275.
4. D. L. DAVIDSON, *Metall. Trans.* **18A** (1987) 2115.
5. M. N. GUNGOR and P. K. LIAW (eds), "Fundamental Relationship Between Microstructure and Mechanical Properties of Metal Matrix Composites" (TMS Warrendale, PA, 1991).
6. J. T. BARNBY and E. SMITH, *Met. Sci. J.* **1** (1967) 1.
7. A. S. ARGON, J. IM and R. SAFOGLU, *Metall. Trans.* **6A** (1975) 825.
8. S. H. GOODS and L. M. BROWN, *Acta Metall.* **27** (1979) 1.
9. F. A. McCLINTOCK, *J. Appl. Mech.* **35** (1968) 363.
10. J. R. RICE and D. M. TRACEY, *J. Mech. Phys. Solids* **17** (1969) 201.
11. W. A. SPITZIG, *Acta Metall.* **38** (1990) 1445.
12. V. TVERGAARD, *ibid.* **38** (1990) 185.
13. J. LLORCA, A. NEEDLEMAN and S. SURESH, *ibid.* **39** (1991) 2317.
14. J. M. PAPAZIAN and P. N. ADLER, *Metall. Trans.* **21A** (1990) 411.
15. S. B. BINER, *Mater. Sci. Eng.* **A156** (1992) 21.
16. A. L. GURSON, PhD thesis, Brown University (1975).
17. *Idem, J. Eng. Mater. Technol.* **99** (1977) 2.
18. V. TVERGAARD, *Int. J. Fract.* **17** (1981) 389.
19. *Idem, ibid.* **18** (1982) 237.
20. V. TVERGAARD and A. NEEDLEMAN, *Acta Metall. Mater.* **32** (1988) 157.
21. C. C. CHU and A. NEEDLEMAN, *J. Eng. Mater. Technol.* **102** (1980) 249.
22. D. PEIRCE, C. F. SHIH and A. NEEDLEMAN, *Compos. Struct.* **18** (1984) 887.
23. A. NEEDLEMAN, *J. Appl. Mech.* **54** (1987) 525.
24. V. TVERGAARD, *Mater. Sci. Eng.* **A125** (1990) 203.
25. A. NEEDLEMAN, *J. Appl. Mech.* **39** (1972) 964.
26. R. E. SMELSER and R. BECKER, in "Abaqus User Conference Proceedings" (Hibbitt, Karlsson and Sorensen, Inc., Pantucket, RI, USA, 1990) p. 207.

Received 24 May
and accepted 29 October 1993